Morphological Study of Melt-Crystallized Poly(ethylene terephthalate). A. Comparison of Transmission Electron Microscopy and Small-Angle X-ray Scattering of Bulk Samples

H. G. Haubruge,*,† A. M. Jonas, and R. Legras

Université catholique de Louvain, Laboratoire de Physique et de Chimie des Hauts Polymères, Croix du Sud 1, B-1348 Louvain-la-Neuve, Belgium

Received August 26, 2003; Revised Manuscript Received November 2, 2003

ABSTRACT: Quantitative image analysis of transmission electron micrographs (TEM) of poly(ethylene terephthalate) (PET) thin sections was performed and compared to data obtained by small-angle X-ray scattering (SAXS) on the same samples. Different methods to analyze the TEM images are presented, and the results are compared with different ways to analyze the SAXS patterns. The results from TEM and SAXS correlate well and lift remaining ambiguities on the semicrystalline morphology formed on cooling from the melt, as a function of the isothermal crystallization temperature. A broad monomodal distribution of lamellar thickness was observed, while no large amorphous gaps were detected. The mean lamellar thickness was shown to be smaller than the mean thickness of amorphous regions, which was also characterized by a broad distribution.

1. Introduction

Since its discovery in 1941,[1] poly(ethylene terephthalate) (PET) has been the subject of countless studies. Its popularity as a research material grew at the same time as it was becoming a commodity product, and along with polyethylene and polypropylene, it became a sort of textbook example for the study of polymer crystallization.[2] It is particularly often considered as a model for the study of the class of semirigid semicrystalline polymers, comprising among others aromatic polyesters, polyamides, and poly(aryl ether ketone)'s; all polymers are characterized by a relatively rigid backbone compared to that of polyethylene.

Because of difficulties to stain differentially such polymers, most previous studies of their semicrystalline morphology were limited to either electron transmission or atomic force microscopy (TEM and AFM) observations on thin films[3−5] or small-angle X-ray scattering (SAXS) studies of bulk samples.[6−10] These methods are not without drawbacks: studies on thin films may be affected by a series of effects arising from confinement, as shown previously.[11,12] On the other hand, analysis of the scattering of X-rays by bulk samples heavily relies on models whose validity still remains to be assessed for semirigid semicrystalline polymers.

For these polymers, the standard two-phase model used to analyze small-angle X-ray scattering data is clearly but an approximation.[13] Results obtained from the electron density correlation function[14] or the interface distribution function (IDF)[15] have to be interpreted in the light of more complex models derived, for instance, from the time or temperature dependence of the semicrystalline morphology. In addition, whereas SAXS unambiguously provides an estimate of the long period (L_p), which is the average interdistance between two successive lamellae in a stack, the situation is more touchy regarding the issue of crystal thickness (l_c), which may be equated to any of two values obtained from the analysis of correlation functions (or, alternatively, of interface distribution functions). Standard analysis[14−16] of such functions indeed provides two lengths, l_1 and l_2 with $l_1 < l_2$ and $l_1 + l_2 = L_p$, corresponding to the thickness of crystals (l_c) and of amorphous interphases (l_a), or vice versa.

This ambiguity fueled recently considerable debate in the literature,[13] resting on two entirely different views of the microstructure of semirigid semicrystalline polymers. In the first interpretation ($l_c = l_1 < l_a = l_2$), the final semicrystalline morphology is composed of homogeneously distributed, space-filling lamellar stacks, with a distribution of thickness for both crystalline and noncrystalline regions. This model also implies that secondary crystallization may occur by the insertion of lamellae in the interlamellar amorphous regions.[9,6,17] It does not preclude, however, the existence of interspherulitic or interfibrillar large amorphous spaces in transient states, where primary crystallization is not complete. In these incompletely crystallized stages, crystalline lamellae could progressively fill space through a stack thickening process.[18]

In the second hypothesis ($l_c = l_2 > l_a = l_1$), lamellar stacks are separated by large gaps of amorphous material even after complete crystallization.[8] Secondary crystallization in these systems results in the formation of multiple populations of lamellae with different thicknesses distributions. These secondary lamellae could grow either by individual insertion in the interstack amorphous regions or by the formation of whole secondary stacks in the same areas.

This uncertainty attached to the assignment of crystalline or amorphous regions to SAXS-measured periodic distances obviously causes large differences in the interpretation of the multiple melting endotherms of PET[9,19,20] or of the amorphous relaxations of PEEK,[21,22,18] for instance. Unfortunately, most studies dedicated to that matter are experimentally based on SAXS and/or differential scanning calorimetry (DSC) only, usually accompanied by a crystallinity measurement, be it by wide-angle X-ray scattering (WAXS), DSC, or densim-

† H. Haubruge is a FNRS Research Fellow.
* Corresponding author.

10.1021/ma0352678 CCC: $27.50
Published on Web 12/06/2003

etry. They are seldom sustained by direct space observations of the underlying morphology and even less often in a quantitative way.

With these considerations in mind, we will focus here on a subset of the problem, namely the morphology resulting from the isothermal crystallization of PET from the melt. In this context, two recent results based both on SAXS measurements and microscopy of melt-crystallized PET, but leading to opposite conclusions, are worth mentioning. On one hand, a strong confirmation of the stack thickening model was provided by a real-time atomic force microscopy (AFM) study, albeit for the free surface of films.[5] On the other hand, the observation of lamellar stacks by transmission electron microscopy (TEM) was interpreted as support for the existence of large interstacks amorphous regions.[4]

The aim of this paper is thus to further investigate the semicrystalline morphology of PET melt-crystallized in the bulk, using TEM and SAXS applied on the very same set of samples. On the basis of adapted staining[23] and image analysis[24] techniques, it provides estimates for the characteristic morphological lengths of PET as a function of its isothermal crystallization temperature. These values are compared to SAXS-derived data and discussed in the light of the existing structural models for this polymer.

2. Experimental Section

Small pellets of PET ($M_n \simeq 20\,000$, grade E47, ICI) were melted at 280 °C for 3 min, cooled at −20 °C/min, isothermally crystallized for 1 h under a nitrogen flow in a Perkin-Elmer DSC7, and then quenched at room temperature. Some samples were also isothermally crystallized from the glass after a heating ramp at 10 °C/min. The final degree of crystallinity was obtained from the DSC thermogram upon heating.[25,26] It was also measured with the aid of a Davenport gradient density column filled with successive concentrations of dissolved NaBr in water. Calibration was obtained using hollow glass beads standards. The density of the original material in pellets form was found to be 1.337 g/cm^3, close to the published value for fully amorphous material.[26] For the computation of crystallinity, reference values for the specific gravity of the crystal and amorphous phases were taken as 1.336 and 1.477 g cm^{-3}, respectively.[25,26]

Transcrystalline structures were observed within the first 50 μm of PET in contact with the aluminum DSC pan, as reported elsewhere.[27] Precautions were taken to avoid these regions during further analysis. The samples were faced using a glass knife and cut at room temperature on a Reichert ultracut equipped with a diamond knife. Ultrathin sections (50−100 nm thick) were deposited on 400 mesh TEM copper grids.

These thin sections were stained by ruthenium tetroxide according to a previously described method.[23] Alternatively, thin sections were also cut from bulk samples exposed to RuO_4 vapor for 6 h. TEM micrographs were obtained on a Philips EM 301 transmission electron microscope operating at 80 kV, of which magnifications were calibrated using an Agar 2160 lines/mm cross grating. Tilt series were also recorded on Tecnai Sphera at 200 kV using a 1K bottom-mount Gatan 791 camera and Tecnai Tomography data acquisition software. The scanned micrographs were analyzed using the Wavemetrics Igor Pro program and custom procedures, except for the Euclidean distance transform which was computed with the ImageJ software from the NIH. Although computations were always made on the original image first, image flattening was also used in order to discriminate lamellar periodicity from long-range variations.[24] To this effect, conservative values of 50 and 2.3 nm for high-pass and low-pass filters spread factors,[24] respectively, were usually applied.

SAXS measurements were performed on the same original bulk samples cut to a 2 mm thickness in a Kratky camera (Anton-Paar KKK) using a Braun OED 50M proportional position sensitive detector and Ni-filtered Cu Kα radiation from a copper anode generator, at room temperature and under primary vacuum. SAXS intensity curves were spline-smoothed, corrected for parasitic scattering, desmeared, and background-subtracted.[18] The computation of the linear correlation function from this signal was described before, as was the extraction of l_1 and l_2 from this function.[8] The interface distribution function was obtained as the second derivative of the correlation function. l_1^{IDF} was obtained as the location of the first maximum of the IDF, L_p^{IDF} as the location of the first minimum of this function, and $l_2 = L_p - l_1$.[15]

In the following results, exponents Bragg, CF, and IDF indicate values obtained from the Bragg peak of the Lorentz-corrected SAXS intensity curve, the correlation function, and the interface distribution function, respectively. Except when stated otherwise, L_p^{CF} is derived from the first subsidiary maximum of the correlation function, while l_1^{CF} is computed as $l_1^{CF} = L_p^{CF}\phi$, where ϕ is the linear crystallinity (or its complementary value according to interpretation). The latter is obtained from the second degree equation $\phi(1 - \phi)L_p^{CF} = r_0$, where r_0 is the intercept of the tangent to the autocorrelation triangle with the abscissa. Let us note that l_1^{CF} could alternatively be obtained as the intercept between the tangent to the autocorrelation triangle and the horizontal line drawn from the first minimum of the correlation function. In our measurements, the value of l_1 evaluated in that way is consistently 2 nm higher than the one based on ϕ.

3. Results

3.1. Crystallinity. SAXS measurements were performed on melt-crystallized samples but also, for completeness, on samples crystallized from the glass at quite low temperatures. However, significant samples could not be obtained in the 150−200 °C crystallization window due to the high crystallization rate of PET in this temperature range. Achievable heating and cooling rates were indeed experimentally limited to ±20 °C/min in the DSC system. For TEM observations, sufficient lamellar contrast could only be obtained for melt-crystallized samples. The low level of order achieved for cold crystallization from the glass at and below 150 °C, and the small lateral extent of crystals particularly,[28] is probably responsible for the lack of discrimination between phases. Annealing from the glass at higher temperatures was not attempted in this work.

Differential scanning calorimetry (DSC) was used to evaluate the degree of crystallinity of the melt-crystallized samples. The difference between melting and crystallization enthalpies on heating, Δh, was obtained by integration of the DSC thermogram along a single linear baseline between temperatures T_1 and T_2 (peak area method), without the need of separate interpolated baselines for crystallization and fusion peaks.[25] The integration bounds were chosen as $T_1 = 100$ °C and $T_2 = 270$ °C. The values found in the literature for the enthalpy of fusion of PET vary considerably (see refs 29 and 30). For our purpose and for increased accuracy, it was evaluated from a published temperature-dependent expression $\Delta H_f(T)$.[26] The weight crystalline fraction could then be expressed as $\chi^{DSC} = \Delta h/\Delta H_f(T_2)$.

Table 1 summarizes the results obtained for samples isothermally crystallized from the melt at varying temperatures, for the same amount of time. The sample crystallized at 240 °C for 1 h is indeed barely crystalline, while the one at 230 °C is characterized by nonspace filling spherulites, as readily checked by optical microscopy under polarized light. For lower crystallization temperatures, down to 200 °C, the semicrystalline

Table 1. Crystallinity of Melt-Crystallized PET Bulk Samples[a]

T_c (°C)	Δh (J/g)	χ^{DSC}	χ^d
240	3.15	0.02	
230	44.75	0.32	0.29
220	59.75	0.43	
210	61.50	0.44	0.43
200	56.15	0.40	0.41

[a]All samples were melt-crystallized for 1 h at T_c on cooling from the melt. DSC (χ^{DSC}) and densimetry (χ^d) results agree fairly well, but the presence of enclosed bubbles precluded density measurements on some samples.

morphology is space-filling, and one notices an almost constant bulk crystallinity, slightly above 40%.

3.2. Long Period. The evaluation of the long period, or an average distance from one crystalline core to the other, is only possible in direct space when a clear differentiation of amorphous and crystalline zones is achieved. For PET, selective staining of the amorphous phase by ruthenium tetroxide gives such a result,[4,23] although the use of osmium tetroxide was also reported in the past.[31] One can argue that crystals could be attacked in the staining process too, but this is irrelevant for the long period as long as some crystalline/amorphous contrast is remaining. However, the validity of the technique to evaluate the lamellar thickness will be discussed later.

The measurement of the characteristic distances of semicrystalline PET by any microscopic technique could also be biased by an inclination of the lamellar stacks toward the direction of observation. Cases where lamellae are strongly inclined are more difficult to discriminate in TEM studies than with the AFM technique which allows the direct viewing of flat-on crystals on the surface.[5] In TEM, one should expect that inclined lamellar stacks would blur and appear as an uniformly uncontrasted zone. Assuming an average cut thickness $d = 70$ nm and $L_p = 12$ nm (a model case consistent with our experimental results), lamellar overlapping resulting in the loss of amorphous−crystalline contrast should already occur for inclinations as small as $\alpha \simeq 10°$ ($\sin(\alpha) = L_p/d$). As a matter of fact, TEM stage tilting on a sample crystallized at 230 °C displays lamellar contrast appearing and disappearing in different areas, for tilt angles along the stack axis in the range 10−15°. However, large zones apparently deprived of lamellae seem experimentally very rare. A short movie of a succession of images obtained on a single cut tilted from −65° to 65° by steps of 2° is available as Supporting Information. In any case, L_p and the other characteristic distances determined from TEM micrographs should not be overestimated by a factor greater than about 1/cos(10°) = 1.015, provided object interfaces are set at midheight between stained and nonstained regions.[12] Figure 1 provides selected images of the lamellar microstructure of PET crystallized from the melt at different temperatures.

The long period of PET lamellar stacks was thus measured concurrently from TEM micrographs and from SAXS measurements according to previously described numerical methods.[24] Figure 2 compares these results as a function of the crystallization temperature T_c. A very good agreement is obviously achieved, with L_p displaying an expected increase with higher T_c. The peculiar decrease observed for the last sample probably results from its degradation due to a longer crystallization time (12 h) at the highest tested temperature (240 °C).

In the case of $T_c = 230$ °C for 1 h, one should recall that the spherulites are not space-filling. A qualitative appreciation of micrographs for this crystallization temperature indicates a greater openness of morphology toward the edge of spherulites, also accounting for larger long periods there than near the core (see Figure 3). As a matter of fact, these regions were not considered in the computation of L_p from TEM images, as they were considered as a possible cause for bias. But even if limited in radius, this open outer shell has a nonnegligible volume when compared to the remaining, more compact, sphere. This might explain why the average long period of the sample is pulled to higher values (still within less than 5% discrepancy) when estimated from SAXS measurements that take into account the whole volume of the sample.

The long periods evaluated by the three available methods to interpret the SAXS display remarkably similar curves, although the order $L_p^{Bragg} > L_p^{CF} > L_p^{IDF}$ is always respected. The absolute difference between results obtained from the correlation function and from the IDF amounts to about 20% on average. This discrepancy results from the different numerical sensitivity of these methods to the distribution of lengths present in the lamellar stacks, somewhat in the same way as number and weight averages differ. Apparently, the average value obtained by TEM is closer to L_p^{Bragg} and L_p^{CF}; the value obtained from the interface distribution function, L_p^{IDF}, underestimates the average TEM long period by about 25%.

3.3. Lamellar Thickness by SAXS. The thickness of amorphous and crystalline regions can be obtained by SAXS within the so-called one-dimensional linear model.[8] This model applies in the case of densely packed, isotropically distributed stacks of parallel lamellae. It is generally accepted when the lateral size and the curvature radius of the crystalline lamellae are much greater than the long period, which is clearly the case in melt-crystallized samples that were observed by TEM. The two distances mentioned in the Introduction, l_1 and l_2, were computed from the correlation and interface distribution functions and are reported in Figure 4.

For cold-crystallized samples, the agreement between the correlation function and the IDF is pretty good. The discrepancies are essentially in the major component l_2, hinting to a broader distribution of the latter. In both cases, the linear crystallinity $\phi = l_c/L_p$ is about 25−30%, or 70−75%, according to the assignment of l_1 or l_2 to the lamellar thickness l_c. This confirms literature data[8,9] but is outside the main scope of this paper.

For melt-crystallized samples, the discrepancies between thicknesses derived from the correlation function and the IDF are important, but the general increasing trend with increasing crystallization temperatures is the same. The interface distribution function yields very close values for l_1 and l_2, with a l_1/L_p ratio slightly less than 50%. On the contrary, the results from the correlation function are more in line with those of cold-crystallized samples, with $l_1/L_p \simeq 30\%$. In both evaluations, l_2 is increasing more strongly than l_1 with T_c. For the sample crystallized at 240 °C for 12 h and most probably degraded, only l_2 is strongly decreasing.

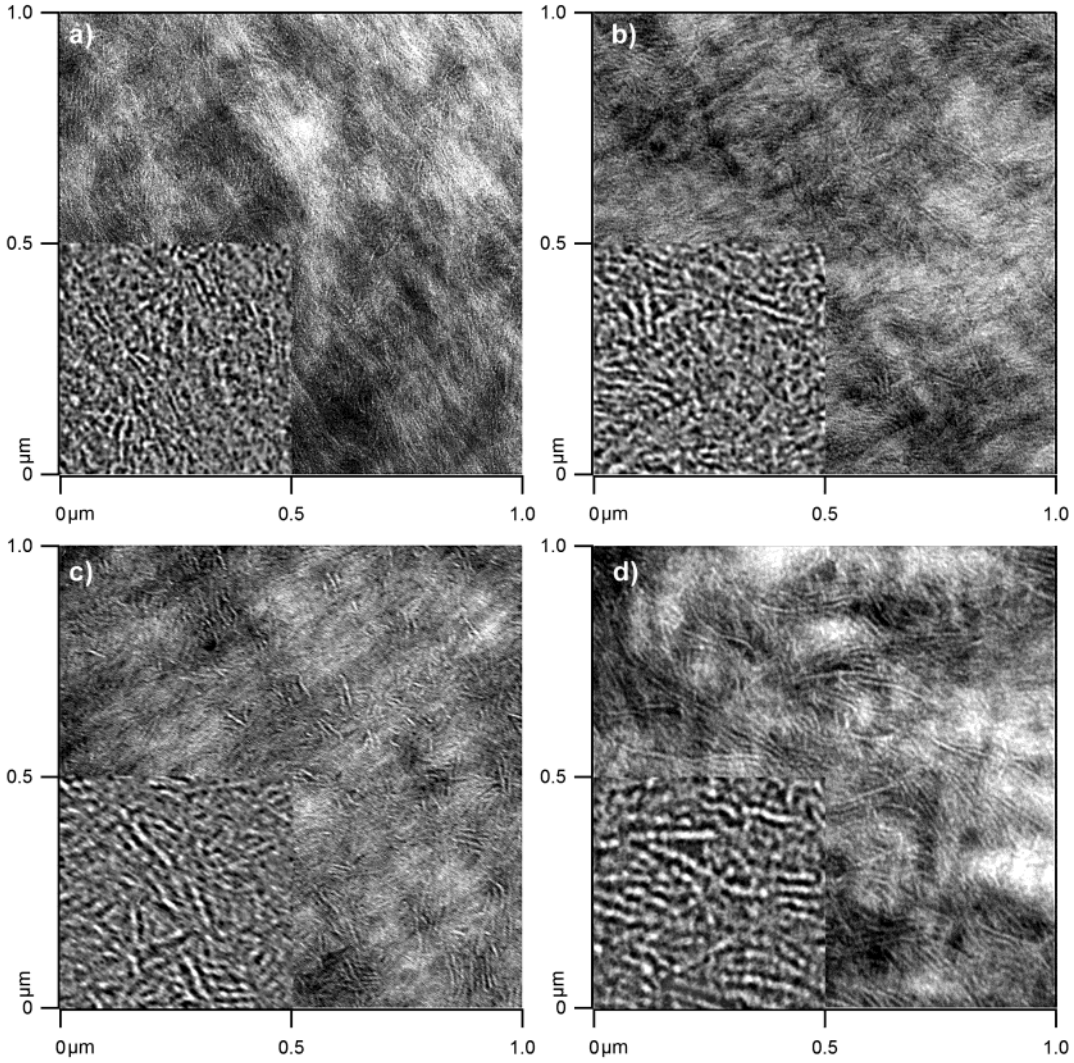

Figure 1. Raw TEM micrographs of stained thin sections from PET bulk samples, crystallized from the melt for 1 h at (a) 200, (b) 210, (c) 220, and (d) 230 °C. Insets are zoomed (×2) and filtered regions of the raw images.

This leads us to the question of the molecular weight dependence of the lamellar morphology. Characteristic distances were measured on PET samples with much lower ($M_w \simeq 12\,000$) and higher ($M_w \simeq 117\,000$) molar masses, as measured by SEC.[23] These results are summarized in Table 2. They should actually be interpreted with caution, since reequilibration of molar masses was shown to take place during melting and recrystallization, even under a nitrogen flow, due to the transesterification ability of PET chains or to the continued polymerization of oligomers (solid-state polymerization). This is made clear by the significant change in molar mass measured after the crystallization procedure. Although sparse, these results indicate that l_2 seems higher for the highest final M_w, while l_1 remains about constant.

As was more fully demonstrated for cold crystallization in time-resolved SAXS experiments,[9,32] the long period also decreases with crystallization time. In the case of melt crystallization at 200 °C, for instance, L_p derived from the SAXS correlation function decreases from 12.8 nm after 5 min of crystallization to 11.5 nm after 1 h (i.e., −10%). The same behavior is observed whatever method is chosen to evaluate L_p, with only minor discrepancies on the absolute decrease (see Table 3). More importantly, analysis by both the correlation function and the interface distribution function shows that this decrease of L_p is entirely linked to the decrease of the major component l_2.

3.4. Lamellar Thickness by TEM. All TEM measurements so far were presented for L_p. The long period is indeed easily evaluated in reciprocal space, as a frequency peak, or in direct space, as a peak-to-peak distance. However, most interest rather focuses on the lamellar thickness l_c and its distribution or the complementary distribution of thickness of the amorphous regions l_a.

3.4.1. TEM Correlation Function. In reciprocal space, a linear correlation function can be computed from the one-dimensional PSD of TEM micrographs.[24] However, because of signal noise, numerical errors accumulation, and the distortion of high frequencies in TEM observations, such an analysis cannot provide very precise lamellar thickness values. Besides, the further derivation of meaningful interface distribution functions is almost impossible. For convenience, l_1^{CF} has to be estimated from TEM-derived correlation functions as the first minimum of the correlation function, which can only result in a slight overestimation. Figure 4 compares the l_1^{CF} values measured by both techniques. Variations of up to 1 nm around the average are observed for

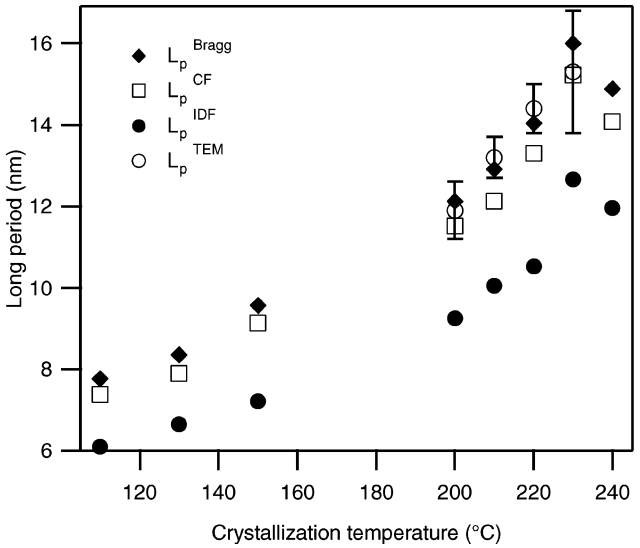

Figure 2. Temperature dependence of the long period of PET. SAXS values of L_p computed from the Bragg peak of the Lorentz-corrected diffraction intensity signal measured on one bulk sample for each crystallization temperature (L_p^{Bragg}) or from the analysis of correlation (L_p^{CF}) and interface distribution (L_p^{IDF}) functions. These samples were either crystallized from the glass (150 °C and below) or from the melt (200 °C and above) for 1 h, except for the sample at 240 °C that was melt-crystallized for 12 h. Estimations from TEM measurements, L_p^{TEM}, are obtained from the one-dimensional power spectral density (1D-PSD) of several micrographs taken on thin sections cut from the same samples used for the SAXS analyses. The standard deviation for SAXS measurements was evaluated at less than 0.2 nm for the 230 °C sample.

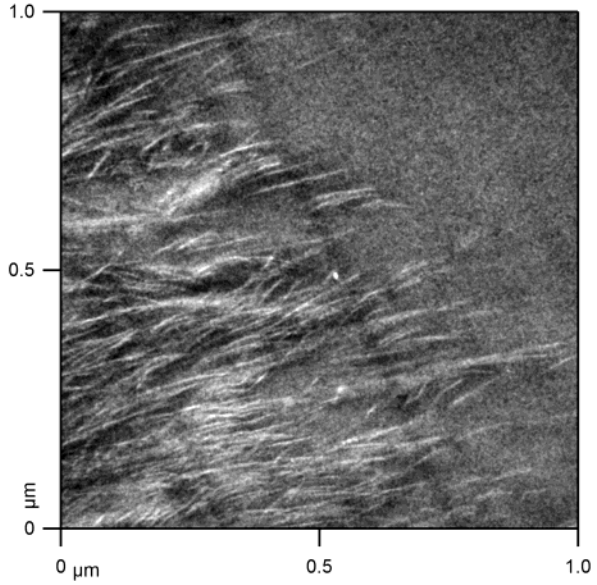

Figure 3. Semicrystalline morphology near the edge of a spherulite (sample melt-crystallized for 1 h at 230 °C). The population of lamellae penetrating in the amorphous region (on the right-hand side) is obviously less dense than in the bulk of the spherulite. The dark diagonal stripes are cut-induced artifacts.

TEM measurements of l_1^{CF}, and TEM- and SAXS-derived correlation functions were found to match only in favorable cases. Despite these discrepancies, the increasing trend of the average l_c with T_c is also clear for TEM-based correlation functions.

It has been suggested that the relatively high concentrations of heavy atoms needed to create electronic contrast would disturb the semicrystalline morphology.[33] Indeed, attack by ruthenium tetroxide can actually also degrade polymer crystals over time, as was shown for PP[34] and POM.[35] However, this only occurs for very long staining times,[34,35] and one may thus consider that the short exposure times used in this study ensure the crystal integrity. Consistent with this assumption, the same average lamellar thickness (within the experimental precision) was observed when staining was performed on bulk samples or directly on thin sections and with varying conditions. In addition, the closeness of SAXS- and TEM-derived long periods indicate negligible swelling of amorphous regions by the stain.

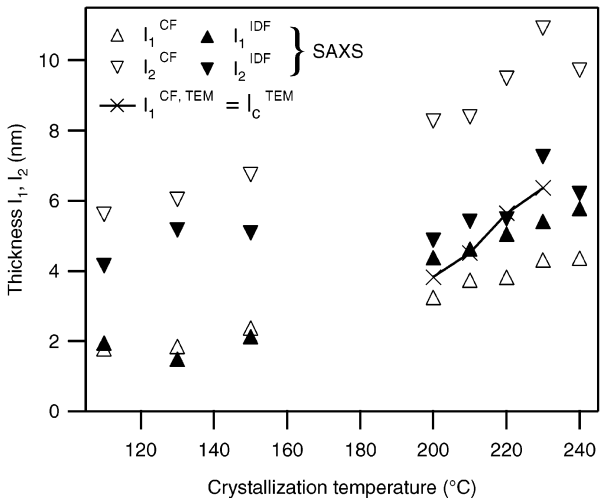

Figure 4. Temperature dependence of the characteristic lengths l_1 and l_2 of semicrystalline PET, derived from SAXS data. The major component l_2 is obtained from the difference of the computed L_p and l_1. The crossed line corresponds to an evaluation of l_1^{CF} from TEM data. The samples are those described in Figure 2.

3.4.2. TEM Chord Distribution Function. As pointed out in the Experimental Section, most of the images used or displayed in this paper were submitted to band-pass filtering in order to remove the long-range fluctuations of the background and the small range nodular noise.[24] As a matter of fact, it is interesting to note that related techniques are finding their way in the analysis of SAXS data, too.[36] Such numerical treatments were also discussed in details for the generalized multidimensional case of scattering.[37] As a second reciprocal space approach, the methods described in the latter paper[37] were applied to TEM micrographs. The chord distribution function (CDF) is computed as the Laplacian of the two-dimensional correlation function of a TEM image. It is equivalent to an interface distribution function in 2D. Figure 5 displays the different steps of this computation and shows the pretty good match that can be achieved between SAXS and TEM results for ideal images as this one. However, one can also see that order is quickly dissipating from the origin in the correlation function and the CDF, and this technique can therefore only be fruitfully applied to well-aligned lamellar stacks to avoid a superposition of orientations. (Some zones of the original image were replaced by its gray level average precisely for that purpose.) In any case, reciprocal space analysis alone, even performed on direct space micrographs, cannot help raising the indetermination on the assignment of l_1 and l_2.

Table 2. Characteristic Dimensions of the Lamellar Microstructure for PET Melt-Crystallized at 230 °C for 1 h as a Function of the Weight-Average Molar Mass[a]

M_w[a] (kg/mol)	L_p^{Bragg} (nm)	L_p^C (nm)	l_1^C (nm)	l_2^C (nm)	L_p^{IDF} (nm)	l_1^{IDF} (nm)	l_2^{IDF} (nm)
42 (45)	16.0	15.2	4.3	10.9	12.7	5.4	7.3
12 (61)	15.8	15.4	4.5	10.9	12.1	5.2	6.9
117 (93)	17.8	17.8	4.9	12.8	13.3	5.4	7.9

[a]The M_w column gives the original M_w of the samples followed, in parentheses, by the M_w measured after crystallization.

Table 3. Characteristic Dimensions of the Lamellar Microstructure for PET Melt-Crystallized at 200 °C for 5 and 60 min

time (min)	L_p^{Bragg} (nm)	L_p^C (nm)	l_1^C (nm)	l_2^C (nm)	L_p^{IDF} (nm)	l_1^{IDF} (nm)	l_2^{IDF} (nm)
5	13.3	12.8	3.4	9.4	9.9	4.3	5.6
60	12.1	11.5	3.3	8.3	9.3	4.4	4.9

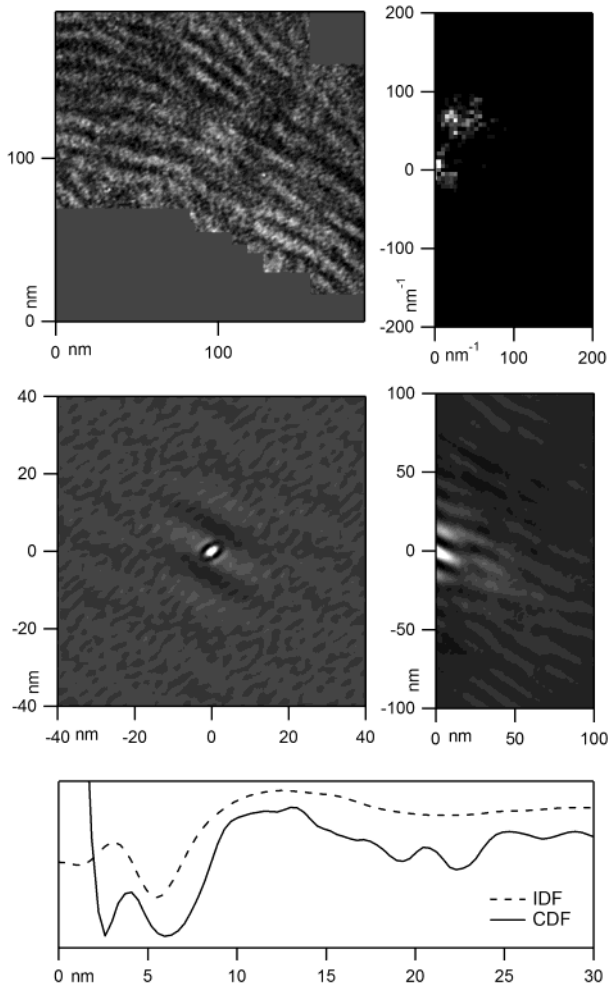

Figure 5. These four images are steps in the computation of the chord distribution function from TEM data. An aligned stack of lamellae was singled out by graying out the surrounding pixels to the average gray level of the stack. Clockwise from top left: flattened TEM image of PET (T_c = 230 °C), power spectral density, 2D correlation function and CDF. The graph below shows the superposition of the SAXS-derived IDF with the CDF profile on a line drawn from the region in perpendicular direction to the stack. The positive peak at the origin of the CDF profile is due to the finite size of the image, while the first negative peak results from the isotropic nodular noise at high frequencies.

3.4.3. Analysis of TEM Images in Direct Space. In direct space, this assignment should be straightforward as soon as a selective contrast between crystalline lamellae and amorphous regions can be achieved. In the case of ruthenium tetroxide staining, the white zones in TEM micrographs are unstained and are therefore unambiguously crystalline. However, the manual measurement of the lamellar thickness is a tedious, time-consuming process and can easily be biased by the human eye sensitivity toward higher contrast. This is particularly the case for PET, where l_c is only a few nanometers large and is close to the important high-frequency noise present in TEM micrographs. For polyethylene[38] or polypropylene[39] where larger lamellae (10 nm or more) are frequently observed, significant results obtained in this way were however reported. Automated procedures in direct space are needed, but they themselves may suffer from some limitations. Automated line profile measurements, for instance, are locally possible for single stacks of well-aligned lamellae[40] but are unfortunately not suitable in the general case of isotropically distributed and very imperfect stacks, as observed in the bulk of pure PET. Despite its statistical poverty, the manual measurement technique was thus used to obtain the distribution of lamellar thickness and long period on a PET micrograph with very clear contrast. Figure 6a displays these results for PET melt-crystallized at 230 °C, the most convenient case for manual measurements. Both distributions are very broad, especially the one for L_p. The average values are l_c = 5.6 nm and L_p = 12.4 nm, the evaluation of L_p from the 1D-PSD of this image being 12.7 nm.

Thresholding is another way to automate image analysis, providing a binarized micrograph consisting of white objects (lamellae) on a black background (amorphous region).[41,42] The different available variants of this technique (iterative, adaptative, fuzzy, etc.) can unfortunately be strongly influenced by the noise in the micrographs. It was therefore only applied to the same fairly ideal micrograph of PET melt-crystallized at 230 °C (see Figure 7). Figure 6b shows the lamellar thickness distribution computed by a particle analysis of the thresholded image. In this procedure, $l_c = 2S/p$, where S is the area and p the perimeter for each particle greater than a given area. Additionally, a rectangularity criterion could be applied to eliminate erroneously detected particles,[5] but this was not applicable here due to an imperfect separation of particles. This should not strongly affect the average l_c, which is 4.5 nm in this case, but is probably responsible for the narrower l_c distribution that is observed.

Alternatively, an Euclidean distance map can also be computed from the binarized image. This results in an image where all feature pixels have a value corresponding to the distance to the nearest background pixel. The local maxima of this map are the ultimate points, which have a value corresponding to half the width of the particle they are in. Figure 6c shows the lamellar thickness distribution computed from the ultimate points population. The average l_c is 4.8 nm, which is probably slightly underestimated due to the consider-

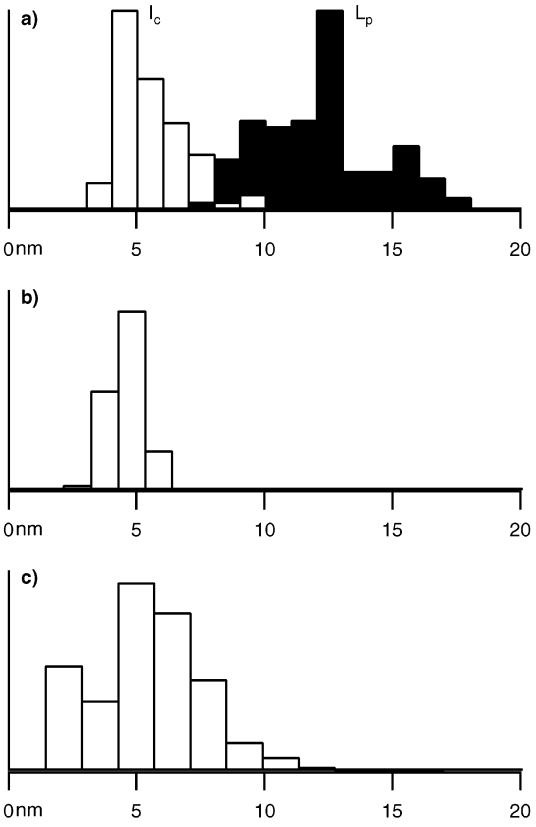

Figure 6. Histograms of size distribution for (a) the crystalline lamellae (white) and the long period (black) obtained from manual gray-level profiles measurements on the flattened image, (b) l_c obtained by particle analysis on the thresholded image, and (c) l_c computed from the ultimate points population of the thresholded image. The original micrograph was obtained on a sample melt-crystallized at 230 °C (see Figure 7).

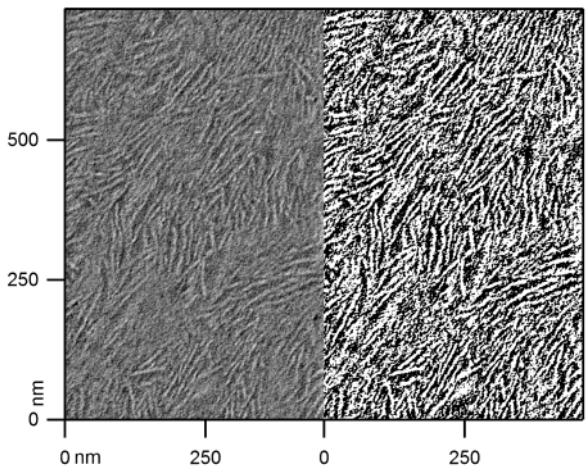

Figure 7. Left: flattened image of PET melt-crystallized at 230 °C (details from the TEM micrograph used for further computations). Right: same image binarized by thresholding. The difficulty to obtain well-separated particles on such images is obvious.

ation of every particles (even very small) by this method.

Let us finally note that related results were obtained for poly(butylene terephthalate) (PBT). PBT proved much more easy to stain than PET, probably due its longer aliphatic segments, also giving a lower glass transition temperature. At high crystallization temperatures, PBT displays lamellae with a very large lateral extent (see Figure 8). For T_c of 200 and 210 °C, the 1D-PSD from TEM micrographs yields L_p of 10.5 and 13.3 nm, respectively. Manual measurements in direct space give $L_p = 11.0$ nm ($l_c = 5.1$ nm) and $L_p = 13.3$ nm ($l_c = 5.6$ nm), respectively. The CDF for $T_c = 200$ °C confirms these values with $L_p = 11.2$ nm and $l_1 = 5.2$ nm.

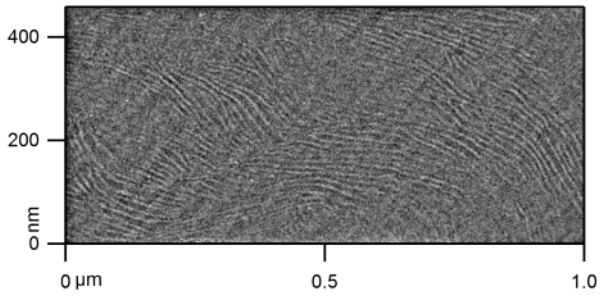

Figure 8. TEM micrograph of PET melt-crystallized at 200 °C.

4. Discussion

4.1. Correlation of TEM and SAXS Data. As a general observation, it can be stated that conceptually equivalent numerical methods applied to TEM and SAXS data provide very similar results. Given direct space images of sufficient quality, some numerical techniques that are much more sensitive to noise (in both high and low frequencies), such as the correlation function or the interface/chord distribution function, can yield results very close to their X-ray scattering counterparts. This confirms the validity of the staining and image analysis procedures.

It has sometimes been argued that the interface distribution function would yield a more accurate evaluation of the characteristic semicrystalline distances (l_c, l_a, and L_p) from X-ray scattering results than the correlation function.[8] Model calculations indeed showed that the IDF is less subject to the superposition of crystalline and amorphous contributions, especially in the case of broad thickness distributions.[8] This statement is however challenged by the fact that the SAXS IDF approach underestimates systematically the TEM-measured long period by about 25%. In this respect, the correlation function or the simple evaluation of the long period by the maximum of the Lorentz-corrected signals provides a better indication of the TEM long period. However, the SAXS IDF does a much better job when used to estimate the minor component l_1 (which will be equated later to crystal thickness), while the SAXS correlation function approach underestimates it rather strongly.

The reasons for these discrepancies undoubtedly lie in the broad distributions of crystal thickness and long period, shown in Figure 6: the high disorder in the lamellar packing of PET is presumably responsible for this extremely broad distribution of lamellar dimensions.[40] Caution should thus be exercised when dealing with average lengths obtained from the analysis of the SAXS of semirigid polymers: these may be off by as much as 25% from the values determined by TEM.

For PET, the problem is even worsened by the fact that the average thickness of the two types of regions, crystalline and amorphous, is so close that the first two negative peaks of the IDF overlap. This loss of information is intrinsically linked to the semicrystalline morphology of the polymer and therefore unavoidable. Nevertheless, these average values still allow the de-

termination of some general trends,[9] such as a clear increase with the crystallization temperature.

4.2. Assignment of l_1: l_c or l_a? Direct space observations have the ability to unambiguously distinguish the crystalline regions from the amorphous ones. From our measurements on PET, and despite some experimental uncertainties, it seems clear that the average thickness of crystals is slightly smaller than the average thickness of amorphous regions, with a linear crystallinity ϕ between 40% and 50%. As a consequence, the minor component l_1 derived obtained from SAXS data should be interpreted as an evaluation of l_c, while the major component l_2 provides an estimate of l_a. For the system crystallized at 230 °C, for instance, l_1 was found by SAXS (IDF approach) to be about 5.4 nm, while the direct space analysis of the images provided values ranging from 4.5 to 5.6 nm. For this sample, L_p was found to be larger than 12 nm whatever the method used to evaluate it. For melt-crystallized PBT also, the values for the long period are not too far from reported SAXS-derived values,[43] but the measurements of l_c performed in direct space indicate that the minor component l_1 should rather be assigned to l_c, too.

The bulk crystallinity of PET, as evaluated by DSC and density measurements, is slightly above 40%, except in the case of noncomplete crystallization where non-space-filling spherulites are formed. Furthermore, no large intraspherulitic gaps (on the order of 200 nm[13]) were detected in any of our TEM observations. This is again totally in line with the morphological results described above. The assignment of l_1 to l_c coupled to a space-filling semicrystalline structure indeed implies that $\phi \simeq \chi$, which is observed. This model is of course only valid when $\chi < 0.5$, but this is at least the case for all melt-crystallized samples used in this study. Furthermore, only one broad distribution of lamellar thickness is observed. Of course, two populations of lamellae, each with its own average thickness but with a broad distribution, could be indiscernible because of the overlap. However, this possibility cannot be assessed with the current evidence.

Another element corroborates the assignment $l_c = l_1$: the increase of the major component l_2 with increasing molar mass. Concerning the molar mass dependence of the semicrystalline morphology, the long period was indeed shown to be proportional to the weight-average dimension r_w of the polymer coils in the melt,[44] crystallinity itself being dependent on $1/r_w$. L_p therefore obeys a law of the form $L_p = l_c + \alpha\sqrt{M_r}$, where l_c is the lamellar core thickness nearly independent of the molecular weight $M_r = r_w^2$ (lying between the moments M_n and M_w of the molar mass distribution), and α is a parameter dependent on the rigidity of the chain in the liquid state before crystallization.[45] Although the results provided in the present work as a function of the molar mass are of limited extent, they indicate a dependence of the major component l_2 only, in the direction expected for l_a. This is in accordance with the assignment of l_2 to the thickness of the interlamellar amorphous regions, which is fully supported by TEM.

5. Conclusions

One of the most currently debated question about semicrystalline semistiff polymers is their crystallization model. We believe that no answer to this question is necessarily universal, so one should bear in mind that the results presented in this paper strictly apply to isothermally melt-crystallized PET only. They can be summarized as follows:

- Given some technical precautions, TEM and SAXS measurements yield very comparable results in terms of both the average lamellar thickness and the average long period. Both characteristic distances increase with temperature, and their distribution is very broad.
- Direct space observations show without ambiguity that l_c is on average slightly smaller than l_a, with a linear crystallinity ϕ about 40%. The distribution of l_c is broad and monomodal. Besides, no large amorphous gaps are detected; i.e., the semicrystalline structure is completely space-filling.
- L_p increases with the molar mass, and this effect mainly arises from a variation of the major component l_2.

As a consequence of these results, we may assign safely the minor component l_1 to the crystalline lamellar thickness in the case of melt-crystallized PET. This is fully compatible with the density measurements, with a bulk crystallinity slightly above 40%. This does however not precludes that l_c could be larger than l_a in the rare cases where the volume crystallinity is superior to 0.5.[10]

Besides, the present work is only valid for the semicrystalline morphology of PET in the bulk. In thin films, melt crystallization of PET in isolated lamellae or in stacks separated by wide gaps can be observed. However, this morphology results from the polymer depletion during crystal growth and the subsequent very small thickness of these interlamellar regions and does not indicate their noncrystallinity, as presented in a following paper.[12]

The quantitative correlation between reciprocal space SAXS measurements and direct space microscopy observations is probably the only way to develop or assess crystallization models with a true physical meaning. However, the techniques presented in this paper leave plenty of room for improvements and the results could easily be extended to various polymer systems and crystallization conditions. In this context, techniques such as the direct observations of the lamellar crystalline core by dark-field imaging and high-resolution transmission electron microscopy (HRTEM)[46,47] seem able to provide a very fine view of the semicrystalline morphology and are therefore very promising.

Acknowledgment. This work was financially supported by the Fonds National de la Recherche Scientifique.

Supporting Information Available: AVI movie consisting of a succession of TEM images obtained on a single microtome tilted from −65° to 65° by steps of 2° (magnification was ×11 500 at 0° tilt; the sample was crystallized for 1 h at 230 °C). This material is available free of charge via the Internet at http://pubs.acs.org.

References and Notes

(1) Whinfield, J. R.; Dickson, J. T. US Patent 2,465,319, 1949.
(2) Wunderlich, B. *Prog. Polym. Sci.* **2003**, *28*, 383.
(3) Lovinger, A. J.; Davis, D. D. *J. Appl. Phys.* **1985**, *58*, 2843.
(4) Xia, Z.; Sue, H. J.; Wang, Z.; Avila-Orta, C. A.; Hsiao, B. S. *J. Macromol. Sci., Phys.* **2001**, *B40*, 625.
(5) Ivanov, D. A.; Amalou, Z.; Magonov, S. N. *Macromolecules* **2001**, *34*, 8944.
(6) Jonas, A. M.; Russell, T. P.; Yoon, D. Y. *Macromolecules* **1995**, *28*, 8491.
(7) Verma, R. K.; Marand, H.; Hsiao, B. S. *Macromolecules* **1985**, *29*, 7767.

(8) Santa Cruz, C.; Stribeck, N.; Zachmann, H. G.; Baltá-Calleja, F. J. *Macromolecules* **1991**, *24*, 5980.
(9) Jonas, A. M.; Russell, T. P.; Yoon, D. Y. *Colloid Polym. Sci.* **1994**, *272*, 1344.
(10) Wang, Z.-G.; Hsiao, B. S.; Fu, B. X.; Liu, L.; Yeh, F.; Sauer, B. B.; Chang, H.; Schultz, J. M. *Polymer* **2000**, *41*, 1791.
(11) Durell, M.; Macdonald, J. E.; Trolley, D.; Wehrum, A.; Jukes, P. C.; Jones, R. A. L.; J., W. C.; Brown, S. *Europhys. Lett.* **2002**, *58*, 844.
(12) Haubruge, H. G.; Daussin, R.; Jonas, A. M.; Legras, R. *Polymer* **2003**, *44*, 8053.
(13) Verma, R. K.; Hsiao, B. S. *Trends Polym. Sci.* **1996**, *4*, 312.
(14) Strobl, G. R.; Schneider, M. J. *J. Polym. Sci., Polym. Phys.* **1980**, *18*, 1343.
(15) Ruland, W. *Colloid Polym. Sci.* **1977**, *255*, 417.
(16) Baltá-Calleja, F. J.; Vonk, C. G. X-ray Scattering of Synthetic Polymers. *Polymer Science Library;* Elsevier: New York, 1989; Vol. 8.
(17) Fougnies, C.; Damman, P.; Villers, D.; Dosière, M.; Koch, M. H. J. *Macromolecules* **1997**, *30*, 1385.
(18) Ivanov, D. A.; Legras, R.; Jonas, A. M. *Macromolecules* **1999**, *32*, 1582.
(19) Kong, Y.; Hay, J. N. *Polymer* **2003**, *44*, 623.
(20) Avila-Orta, C. A.; Medellí-Rodríguez, F. J.; Wang, Z.-G.; Navarro-Rodrígueza, D.; Hsiao, B. S.; Yeh, F. *Polymer* **2003**, *44*, 1527.
(21) Jonas, A. M.; Legras, R. *Macromolecules* **1993**, *26*, 913.
(22) Sauer, B. B.; Hsiao, B. S. *Polymer* **1995**, *36*, 2553.
(23) Haubruge, H. G.; Jonas, A. M.; Legras, R. *Polymer* **2003**, *44*, 3225.
(24) Haubruge, H. G.; Gallez, X.; Nysten, B.; Jonas, A. M. *J. Appl. Crystallogr.* **2003**, *36*.
(25) Blundell, D. J.; Beckett, D. R.; Willcocks, P. H. *Polymer* **1981**, *22*, 704.
(26) Séguéla, R. *Polymer* **1993**, *34*, 1761.
(27) Sajkiewicz, P.; Carpaneto, L.; Wasiak, A. *Polymer* **2001**, *42*, 5365.
(28) Groeninckx, G.; Reynaers, H.; Berghmans, H.; Smets, G. *J. Polym. Sci., Polym. Phys. Ed.* **1980**, *18*, 1311.
(29) Jog, J. P. *J. Macromol. Sci., Rev. Macromol. Chem. Phys.* **1995**, *C35*, 531.
(30) Bicerano, J. *Rev. Macromol. Chem.* **1998**, *C38*, 391.
(31) Watkins, N. C.; Hansen, D. *Text. Res. J.* **1968**, *32*, 388.
(32) Wang, Z.-G.; Hsiao, B. S.; Sauer, B. B.; Kampert, W. G. *Polymer* **1999**, *40*, 4615.
(33) Sundararajan, N.; Obendorf, S. K. *J. Polym. Sci., Part B: Polym. Phys.* **1998**, *36*, 1443.
(34) Li, J. X.; Cheung, W. L. *J. Appl. Polym. Sci.* **1999**, *72*, 1529.
(35) Li, J. X.; Ness, J. N.; Cheung, W. L. *J. Appl. Polym. Sci.* **1996**, *59*, 1733.
(36) Stribeck, N. *Colloid Polym. Sci.* **2002**, *280*, 254.
(37) Stribeck, N. *J. Appl. Crystallogr.* **2001**, *34*, 496.
(38) Strobl, G. R.; Schneider, M. J.; Voigt-Martin, I. G. *J. Polym. Sci., Polym. Phys.* **1980**, *18*, 1361.
(39) Yamada, K.; Hikosaka, M.; Toda, A.; Yamazaki, S.; Tagashira, K. *Macromolecules*, in press.
(40) Ivanov, D. A.; Pop, T.; Yoon, D. Y.; Jonas, A. M. *Macromolecules* **2002**, *35*, 9813.
(41) Pratt, W. K. *Digital Image Processing*, 2nd ed.; John Wiley: New York, 1991.
(42) Castelman, K. R. *Digital Image Processing;* Prentice Hall: Englewood Cliffs, NJ, 1996.
(43) Hsiao, B. S.; Wang, Z.-G.; Yeh, F.; Gao, Y.; Sheth, K. C. *Polymer* **1999**, *40*, 3515.
(44) Rault, J.; Robelin, E.; Perez, G. *J. Macromol. Sci., Phys.* **1983**, *B22*, 575.
(45) Robelin-Souffaché, E.; Rault, J. *Macromolecules* **1989**, *22*, 3581.
(46) Fujita, M.; Tsuji, M.; Kohjiya, S. *Macromolecules* **2001**, *34*, 7724.
(47) Tsuji, M.; Fujita, M.; Shimizu, T.; Shinzo, K. *Macromolecules* **2001**, *34*, 4827.

MA0352678